Mechanisms of abnormal grain growth in friction-stir-welded aluminum alloy 6061-T6

Alexander Kalinenko [a], Vasiliy Mishin [b], Ivan Shishov [b], Sergey Malopheyev [a], Ivan Zuiko [a], Vseslav Novikov [a,c], Sergey Mironov [a,*], Rustam Kaibyshev [a], Sheldon Lee Semiatin [d]

[a] Belgorod National Research University, Pobeda 85, Belgorod 308015, Russia
[b] Peter the Great St. Petersburg Polytechnic University, Polytechnicheskaya 29, St-Petersburg 195251, Russia
[c] Belgorod State Technological University named after V.G. Shukhov, Kostyukova 46, Belgorod 308012, Russia
[d] MRL Materials Resources LLC, Xenia Township, OH 45385, USA

ARTICLE INFO

ABSTRACT

The relationship between the temperature conditions during friction-stir welding (FSW), the stir-zone micro-structure, and the thermal stability of welded aluminum-alloy 6061 joints was established. To facilitate inter-pretation of the microstructural data, temperature distributions generated during FSW were quantified using a finite-element-modeling (FEM) approach. In all cases, the stir-zone microstructure was found to be unstable against abnormal grain growth (AGG) during post-weld solution annealing. Moreover, it was found that AGG always developed very rapidly, being nearly complete during heating of the welded material from ambient condition to the solution temperature. In all welded conditions, annealing behavior followed Humphrey's cellular-growth model. In particular, for low-heat-input conditions, a combination of a fine-grain structure and a low content of secondary particles gave rise to a competition between normal grain growth and AGG. As a result, the final grain size was relatively small. By contrast, high-heat-input conditions gave rise to a combination of relatively-coarse grains and a high fraction of particles in the weld nugget, which provided microstructural stability. However, a fine-grain surface layer associated with the tool shoulder triggered catastrophic grain coarsening that eventually consumed the entire weld zone and resulted in millimeter-scale grains. Remarkably, AGG led to a 40° $\langle 111 \rangle$ rotation of the crystallographic texture in the stir zone. It was thus concluded that the AGG was governed by at least two mechanisms, viz., the pinning effect exerted by second-phase particles and the enhanced mobility of $40^{\circ} < 111 >$ boundaries.

1. Introduction

The relatively-low stability of joined materials against abnormal grain growth (AGG) is sometimes considered one of the most significant drawbacks of the friction-stir welding (FSW) technique [1]. This phenomenon involves the catastrophic coarsening of a few grains, which eventually consume almost the entire weld zone. This undesirable effect[1] has been reported to occur in various structural materials, including aluminum alloys [2–22], magnesium alloys [23–25], steels [26–29], and even metal-matrix composites [30,31], thus suggesting that it is an intrinsic characteristic of FSW.

The problem of AGG in FSW joints appears to be most prominent for heat-treatable aluminum alloys. In these alloys, FSW often leads to the dissolution of second-phase particles [32–49] and a concomitant loss of strength. To recover such properties, these alloys must then undergo a post-weld heat treatment comprising solution annealing followed by artificial aging. The first step of this treatment usually gives rise to catastrophic grain coarsening, which was observed to occur in 2xxx [6,7,13], 6xxx [12,14,22], and 7xxx [2,3,16] series aluminum alloys, and typically led to considerable degradation of weld properties [16,50]. AGG in such cases is often explained in terms of Humphreys' cellular-growth model [2,3,5,6,9,10,17,20,31]. According to this theory, catastrophic microstructural coarsening is attributed to the synergetic effect of significant grain refinement and dissolution of secondary

---

* Corresponding author.
  E-mail address: mironov@bsu.edu.ru (S. Mironov).

[1] It should be emphasized that AGG may be beneficial for several applications, including electrical conductivity in silicon steels, creep resistance in refractory metals, etc. In friction-stir welding/processing, however, AGG is usually considered to be undesirable due to a degradation of material strength and/or ductility.

particles which occur during FSW [51,52].

It was also found that microstructural stability against AGG depends on the weld heat input [2]. Specifically, a lowering of the FSW temperature usually enhances the grain-refinement effect and thus produces a fine-grained microstructure, which is not be stabilized by constituent particles [2]. An increase in welding temperature provides microstructural coarsening, thereby reducing the driving force for grain growth [2]. However, high-temperature FSW conditions may also result in a substantial thermal gradient across the weld thickness, thus giving rise to an inhomogeneous microstructure distribution. In turn, this may trigger AGG, which is most pronounced in relatively-thick welds [2,16]. In such cases, the abnormal grains typically nucleate at either the upper weld surface or the weld root, and then grow toward the rest of the stir zone [2–6,8,10,13,20,21,23,24,28]. To equilibrate the temperature distribution within the stir zone (and thus eliminate a prerequisite for AGG), a low-thermal-conductivity backing plate has recently been recommended to use for FSW [16]. It is also worth noting that the annealing behavior may be sensitive to heating rate. Specifically, rapid heating may lead to suppression of AGG [2].

It is important to emphasize that the FSW processing window for aluminum alloys is relatively broad, and thus the welding temperature may vary over a wide range [53]. Hence, the current concept of particle behavior during FSW, characterized largely by particle dissolution in the stir zone, appears to be oversimplified. For example, particle coarsening (instead of dissolution) may be an important mechanism during *low-heat-input* FSW [54]. Considering the comparatively low cooling rate during high-heat-input FSW, on the other hand, it may be possible that dissolved particles may partially re-precipitate during the weld cooling cycle [16,32,55]. The complexity of particle behavior during welding may be an additional factor which governs AGG together with the grain size. To the best of the authors' knowledge, however, this matter has been not studied systematically.

Another circumstance which may affect the occurrence of AGG was a recent finding that it occurs mainly during the *heat-up* portion per se of solution treatment, i.e., during heating from ambient conditions to the solution temperature [56,57]. If this is indeed the case, clarification of the fundamental mechanism(s) of AGG are therefore still needed.

The objective of the present research, therefore, was to generalize such new findings and thus shed more light on AGG in friction-stir welds. To this end, the emphasis of the present work was the elucidation of the relationship between the weld heat input, the FSW-induced microstructure, and subsequent annealing behavior of FSW joints. Moreover, particular attention was paid to microstructure changes during the heating stage of post-weld heat treatment.

2. Material and experimental procedures

2.1. Material

The material used in the present research was commercially-produced aluminum alloy 6061 supplied as a hot extruded bar. This is a typical heat-treatable aluminum alloy that is widely used in the transportation industry and whose FSW behavior is known relatively well. The measured chemical composition of the as-received material (in wt%) was 0.88 Mg, 0.66 Si, 0.72 Fe, 0.26 Cu, 0.12 Mn, 0.12 Cr, 0.09 Zn, the balance being Al. To obtain a precipitation-hardened (T6) condition, the material was solution annealed at 550 °C for 1 h, water quenched, and then aged at 160 °C for 8 h. The heat-treated material was characterized by millimeter-size grains elongated along the extrusion axis, a relatively strong $\langle 111 \rangle + \langle 110 \rangle$ fiber texture, and a high density of nano-scale β'' particles evenly distributed within the grain interiors (supplementary Fig. S1). Throughout the manuscript, this material condition is denoted as the *base material*.

2.2. FSW procedure and post-weld heat treatment

Sheets of the base material measuring 3 mm in thickness were extracted from the bar and butt-welded along the extrusion direction using a commercial AccurStir 1004 FSW machine. The welding tool was manufactured from carbon steel and had a conventional design consisting of a concave-shaped shoulder 12.5 mm in diameter and a threaded M5 cylindrical probe 2.7 mm in length (supplementary Fig. S2a). To examine the possible influence of FSW heat input, two different welding trials were conducted (Table 1). These were designed on the basis of previous experiments [54] and are denoted subsequently as the "low-heat-input condition" and "high-heat-input condition". In all cases, FSW was performed employing the plunge-depth control mode (with the plunge depth of 2.8 mm), a tool tilt angle of 2.5°, and a stainless steel backing plate. The typical appearance of welded material is shown in supplementary Fig. S2b. The usual convention of FSW geometry was adopted with WD, ND, and TD being the welding direction, normal direction, and transverse direction, respectively.

To measure the thermal cycle during FSW, type-K thermocouples were placed in the heat-affected zone as well as in close proximity to the stir-zone border (supplementary Fig. S3). In the latter case, the temperature was measured at two locations – near the upper surface of the stir zone and at the weld mid-thickness.

To establish the effects of the post-FSW heat treatment on microstructure evolution, the welded specimens were placed in a muffle furnace heated to a solution temperature of 540 °C, and their thermal history was recorded continuously (Fig. 1). When a particular specimen was heated to a desired/specified peak temperature (i.e., 350 °C, 400 °C, 425 °C, 450 °C, 500 °C, 525 °C, or 540 °C), it was immediately quenched in water to preserve the evolved microstructure.

2.3. Microstructural examinations

Microstructural observations were conducted using electron backscatter diffraction (EBSD), backscatter electron scanning microscopy (BSE-SEM), and transmission electron microscopy (TEM) techniques. EBSD and BSE-SEM examinations were conducted in the weld cross-section (i.e., ND × TD) plane. In both cases, an appropriate surface finish was obtained using conventional metallographic techniques, with the final step comprising long-term (24-h) vibratory polishing in a colloidal silica suspension. For the TEM investigation, microstructure specimens were machined from the WD × TD plane, and the final surface was produced by electropolishing in a solution of 25% nitric acid in ethanol.

To facilitate interpretation of microstructural changes, thermodynamic calculations were performed employing ThermoCalc 2020a software with the TCAl1 database.

To provide a broad view of the microstructure distribution within welded specimens, Vickers microhardness profiles were acquired across the weld mid-thickness by applying a load of 200 g with a dwell time of 10 s using a Wolpert 402MVD microhardness tester.

To minimize the possible influence of natural aging on microstructure, all samples were stored in a freezer at −18 °C prior to examination.

Table 1
FSW conditions used in the present work.

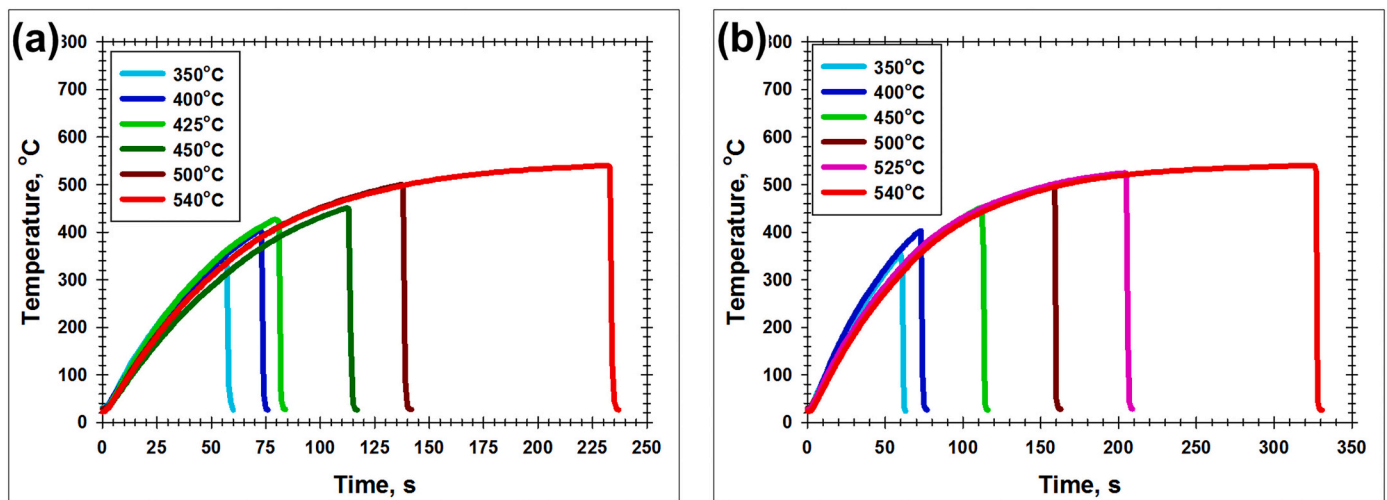| FSW condition	Tool rotation rate (N), rpm	Tool travel speed (V), mm/min	Linear heat input (N/V), m^{-1} [58]	Heat index (N^2/V), (ms)$^{-1}$ [58]
Low-heat-input FSW	500	380	1.3×10^3	1.1×10^4
High-heat-input FSW	1100	125	8.8×10^3	1.6×10^5

Fig. 1. Temperature-time diagrams for post-weld annealing of (a) the low-heat-input condition, and (b) the high-heat-input condition to different peak temperatures.

2.3.1. EBSD measurements

EBSD analysis was performed employing an FEI Quanta 600 field-emission-gun scanning electron microscope (FEG-SEM) equipped with TSL OIM™ software and operated at an accelerated voltage of 20 kV. To provide thorough insight into microstructural changes, sample-scale EBSD maps were acquired across the entire weld zone. Scan step sizes of 1 μm or 5 μm were used for as-welded and annealed materials, respectively. For detailed microstructural examination in particular areas of interest, additional EBSD maps were obtained with a scan step size of 0.2 μm. Furthermore, to enhance the reliability of EBSD data, fine grains comprising two or fewer pixels were automatically "cleaned" from the maps by employing the standard grain-dilation option of the EBSD software. Considering the limited angular accuracy of EBSD, a lower-limit misorientation cut-off of 2° was applied. A 15° criterion was used to differentiate low-angle boundaries (LABs) from high-angle boundaries (HABs). The grain size was measured using the equivalent-grain-diameter approach, i.e., by assuming each grain as a circle of equivalent area and calculating the associated diameter [59].

2.3.2. BSE-SEM and TEM observations

BSE-SEM and TEM were used to quantify the nature of second-phase particles. For BSE-SEM, observations were conducted with the FEI Quanta 600 FEG-SEM operating at an accelerated voltage of 20 kV. The acquired BSE micrographs were analyzed using Digimizer software. Due to the penetration of the electron beam into the material depth, the acquired images also showed particles lying below the specimen surface. To exclude those from consideration, the micrographs were subjected to careful watershed segmentation in order to differentiate the particles from the matrix phase as well as surface particles from the subsurface particles. The particle size was also quantified using the equivalent-diameter method. TEM particle observations were conducted with a JEOL JEM-2100EX transmission electron microscope operated at 200 kV. To enhance the contrast associated with particles of β″ phase, TEM specimens were typically tilted to align the incident electron beam with a ⟨100⟩ zone axis.

The particle-size distributions measured by TEM and BSE-SEM were found to broadly overlap each other (supplementary Fig. S4). Hence, considering the superior statistics of BSE-SEM over TEM, the former approach was selected for quantitative particle analysis.

3. Numerical simulations

Considering the difficulty in the direct measurement of temperatures within the stir zone, numerical 3D FEM simulations of FSW were also formulated and performed. A brief description of the approach is given in the present section; a more detailed explanation is provided in the supplementary materials. In particular, fully-coupled DEFORM-3D simulations were conducted; i.e., temperature and strain were calculated simultaneously after each time increment. The simulations included a workpiece, a welding tool, and a backing plate (supplementary Fig. S5a). To provide an appropriate balance between the calculation accuracy and the calculation time, a non-uniform FEM mesh was used (supplementary Fig. S5a). Moreover, to avoid excessive distortion of the mesh elements due to the severe deformation conditions characteristic of FSW, an adaptive re-meshing approach was employed per the work by Wan, et al. [60]. The temperature field was thus calculated for the entire workpiece being welded. For further analysis, however, the temperature distribution in the weld section directly behind the tool probe (supplementary Fig. S5b) was extracted from the model calculations.

The welded material (AA6061-T6) was treated as a perfectly-plastic body, whose constitutive behavior was quantified using the Johnson-Cook formulation [61]. The welding tool and the backing plate were assumed to be rigid bodies. The contact condition between the workpiece and the welding tool was assumed to follow the shear friction model. Total heat generation was considered to arise from frictional heating and deformation-induced heating. In addition, heat transfer from the surface of the welding tool to the workpiece material was taken to follow Fourier's law of heat conduction, and heat loss from the workpiece surfaces to the surroundings was considered to be due to free convection, radiation, and heat transfer into the backing plate.

The relatively good agreement between predicted and measured thermal cycles (supplementary Fig. S6) and normal Z-forces (supplementary materials) tended to corroborate the overall validity of the input data and simulation formulation.

4. Results

4.1. FSW thermal cycle

Typical thermal cycles measured at the edge of the stir zone (Fig. 2) revealed, as expected, that the high-heat-input weld was characterized by a comparatively-high peak temperature. Moreover, this welding condition also provided a relatively-low cooling rate. As shown in previous work [54], this effect was primarily associated with the low feed rate of the welding tool.

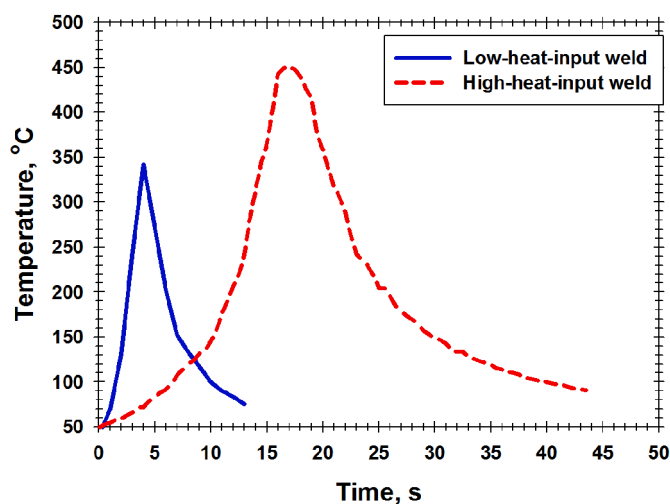Insight into the temperature field *within* the stir zone was obtained

Fig. 2. Typical thermal cycles measured during FSW at the edge of the stir zone at the weld mid-thickness.

from the numerical simulations[2] (Fig. 3). In accordance with expectations, the predicted temperature distribution was not uniform. In addition to the thermal gradient in the width direction of the weld, an increased temperature at the upper surface of the stir zone was also observed. The latter effect is well known in FSW, usually being attributed to the dominant role played by the tool shoulder in heat generation [62].

To obtain a more-detailed idea of the temperature distributions, profiles along the weld mid-thickness were derived from the simulations (Fig. 4a). For illustrative purposes, the tool-probe diameter and the tool shoulder diameter were included in such profiles. To a first approximation, these two delineate the stir zone and the heat-affected zone, respectively. Of particular interest was the observation that the temperature on the advancing side (AS) of the weld was slightly higher than that on its retreating side (RS). This asymmetry of the temperature profile has been well described previously [63–70], and is usually associated with specific characteristics of metal flow during FSW.

A comparison of Fig. 4a and Fig. 2 showed that the simulated peak temperature in the stir zone was ~50 °C higher than the measured one. In the context of particle dissolution, such a difference may be of critical importance. Specifically, Fig. 4b provided evidence that the predicted temperature in the stir zone was high enough for complete dissolution of the constituent Mg_2Si (i.e., β-phase) particles in the high-heat-input weld. By contrast, lower temperatures and the retention in the stir zone of a significant volume fraction of the second phase were predicted for the low-heat-input weld.

4.2. Microstructure in the as-welded state

4.2.1. Grain structure

EBSD inverse-pole-figure maps (Figs. 5 and 6) and the associated microstructural statistics (Table 2) revealed that FSW resulted in the formation of a fine-grain microstructure with a significant fraction of LABs in the stir zone for both welded samples. Such microstructures are often found in friction-stirred aluminum alloys and are usually associated with the occurrence of continuous recrystallization in the highly-strained stir zone [71].

As expected, the low-heat-input weld was characterized by a

relatively fine-grain microstructure (Table 2). The high-heat-input weld exhibited a comparatively low HAB fraction. As previously proposed [72,73], the latter effect was likely a result of enhanced recovery during *higher-temperature* FSW. The higher temperatures would tend to reduce dislocation density (resulting in lower flow stresses) and thus retard the progressive evolution of deformation-induced boundaries.

Considering the increased welding temperature on the AS of the stir zone (Fig. 4a), it was of interest to examine the microstructure that evolved in this area. EBSD measurements (Fig. 5c) showed that the microstructure of the low-heat-input weld was characterized by a somewhat finer grain size (Table 2). The possible origin of this phenomenon is discussed in the following section. On the other hand, no such effect was found on the AS of the high-heat-input sample (not shown).

A fine-grain structure with an increased LAB fraction was also found at the upper surface of the stir zone (e.g., Fig. 6b, Table 2). In FSW, such a surface layer is usually associated with deformation imposed by the tool shoulder [74]. The fine-grain character of microstructure in this area was likely a result of the relatively high strain and strain rate associated with the tool shoulder, despite the relatively high FSW temperature predicted in this area (Fig. 3). In the present study, the fine-grain surface layer was most pronounced in the high-heat-input weld (Fig. 6b and supplementary Fig. S7).

4.2.2. Second-phase particles

BSE-SEM examination of stir-zone material at relatively low magnifications revealed a nearly-random distribution of second-phase particles in both welded conditions (Fig. 7 and supplementary Fig. S8). Moreover, there was no preferential clustering the particles at grain boundaries. On the other hand, TEM showed that the particles were often concentrated within regions with significant dislocation substructure (Figs. 8a, b). In all cases, the particles had a nearly equiaxed morphology (Figs. 8a, b and supplementary Fig. S9) and a mean size of ~60 nm (Table 2). The observation that the fine particles in the high-heat-input weld frequently exhibited Moire fringe contrast (Fig. 8c) was suggestive of a semi-coherent relationship with the matrix.

It is important to note that the particles were found in both welded conditions despite ThermoCalc predictions of complete dissolution in the high-heat-input weld (Fig. 4b). Moreover, statistical analysis showed that the volume fraction of particles in the high-heat-input weld was higher than that in the low-heat-input condition (Table 2), and the particle-size distribution of the former condition was skewed toward the finest particles (Fig. 9a). This somewhat surprising result was corroborated by microhardness measurements which showed a comparatively high strength of the stir-zone material[3] in the high-heat-input weld (Fig. 9b). To rationalize the experimental results and the ThermoCalc predictions, it can be hypothesized that the particles in the high-heat-input weld had initially dissolved during FSW but then partially re-precipitated during the cooling cycle. The re-precipitation effect was likely a result of the low cooling rate associated with this FSW condition (Fig. 2). Considering the TEM observations (Fig. 8), it seems that the re-precipitation occurred preferentially within the dislocation structure thus leading to an inhomogeneous particle distribution.

In contrast, the particles in the low-heat-input weld were obviously not dissolved completely (Fig. 4b). Moreover, given the relatively-high cooling rate (Fig. 2) and an increased proportion of relatively coarse particles in this welding condition (Fig. 9a), it was unlikely that gross particle re-precipitation occurred during the weld cooling cycle. Hence, the particle behavior was presumably governed by the coarsening mechanism.

Thus, considering the essential difference in the particle behavior

---

[2] To simplify the simulation procedure, fine-scale meshing had been applied only for a limited area of the welded workpiece. As a result, some details related to the formation of weld flash were neglected. This led to some inaccuracy in the simulated shape of the weld upper surface.

[3] To a first approximation, the stir zone in Fig. 9b was located within the area outlined by the probe diameter. The edges of the tool shoulder indicated the heat-affected zone.
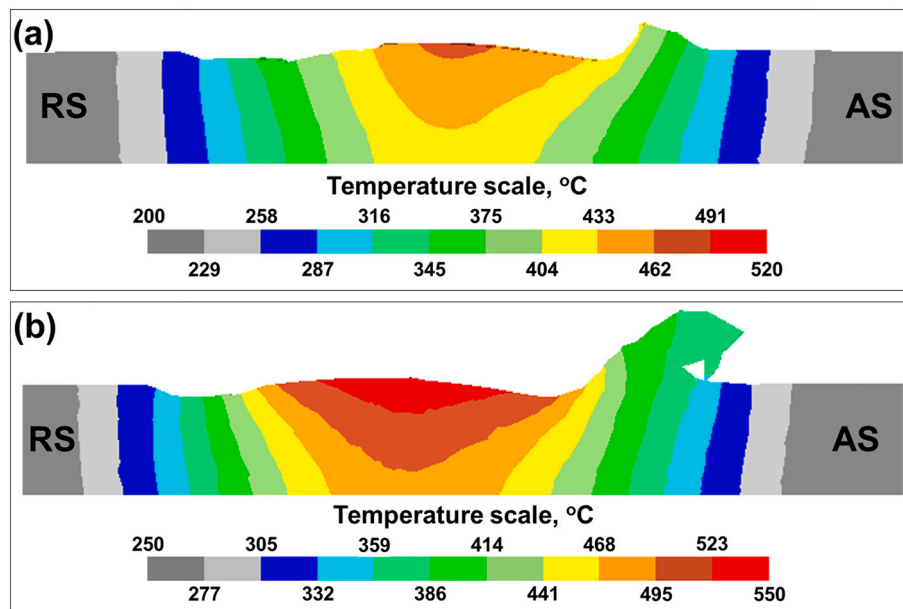
Fig. 3. Two-dimensional temperature distributions predicted from numerical simulations for (a) the low-heat-input weld and (b) the high heat-input weld. RS and AS denote the retreating and advancing sides, respectively.
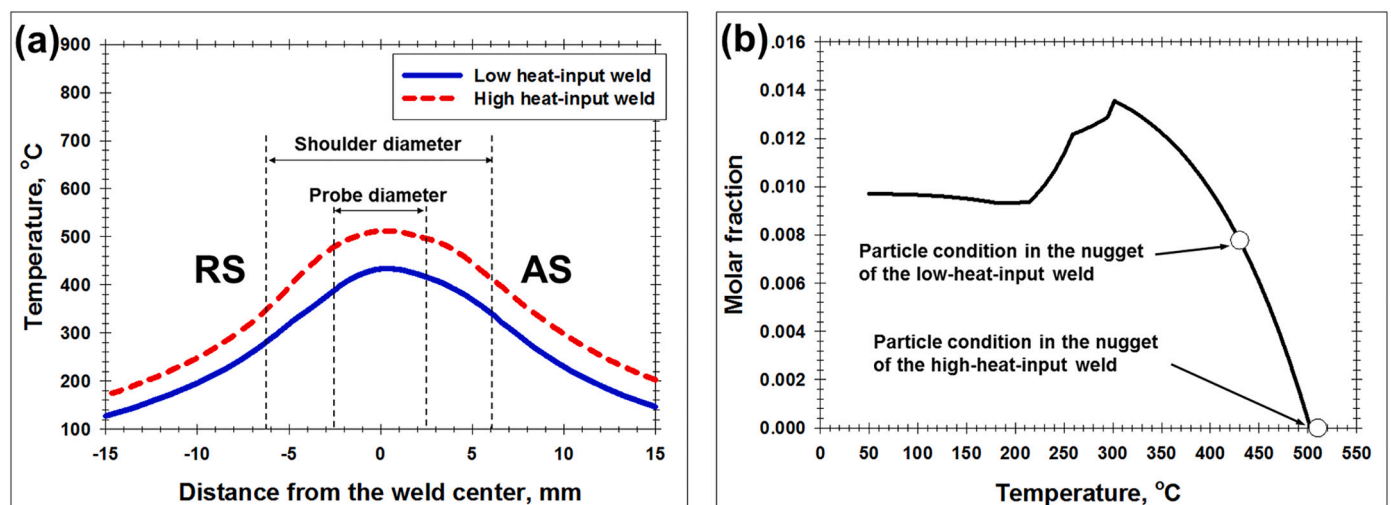

Fig. 4. (a) Temperature profiles along the weld mid-thickness derived from the simulation results shown in Fig. 3, and (b) ThermoCalc prediction of the temperature dependence of the molar fraction of Mg_2Si (i.e., β-) phase.

observed in the present work, the term "low-heat-input condition" could be defined as that assuming the prevalence of a particle-coarsening mechanism. In contrast, the term "high-heat-input condition" implied complete particle dissolution during FSW and then partial re-precipitation during the weld cooling cycle.[4]

In the low-heat-input weld, an increased concentration of secondary particles on the AS of the stir zone (Table 2) was also worthy of remark. This observation agreed well with a measurable hardening effect observed in this area (arrow in Fig. 9b). In previous work [5], a similar effect was attributed to wear of the welding tool during FSW. Although this phenomenon rarely occurs in aluminum alloys, it may perhaps take place under low-temperature conditions. If so, the resulting tool debris should increase the apparent particle volume fraction in this area (Table 2). On the other hand, it should be emphasized that tool wear was not confirmed experimentally in the present study, and thus the above suggestion warrants further investigation.

4.3. Annealing behavior

In several recent studies [56,57], it has been reported that AGG in friction-stir welded heat-treatable alloys may occur during the heating stage of solution heat treatment. To provide a clearer view of this phenomenon, the present study focused on more-detailed observations of microstructure changes during the heating of welded material from ambient conditions to the solution temperature.
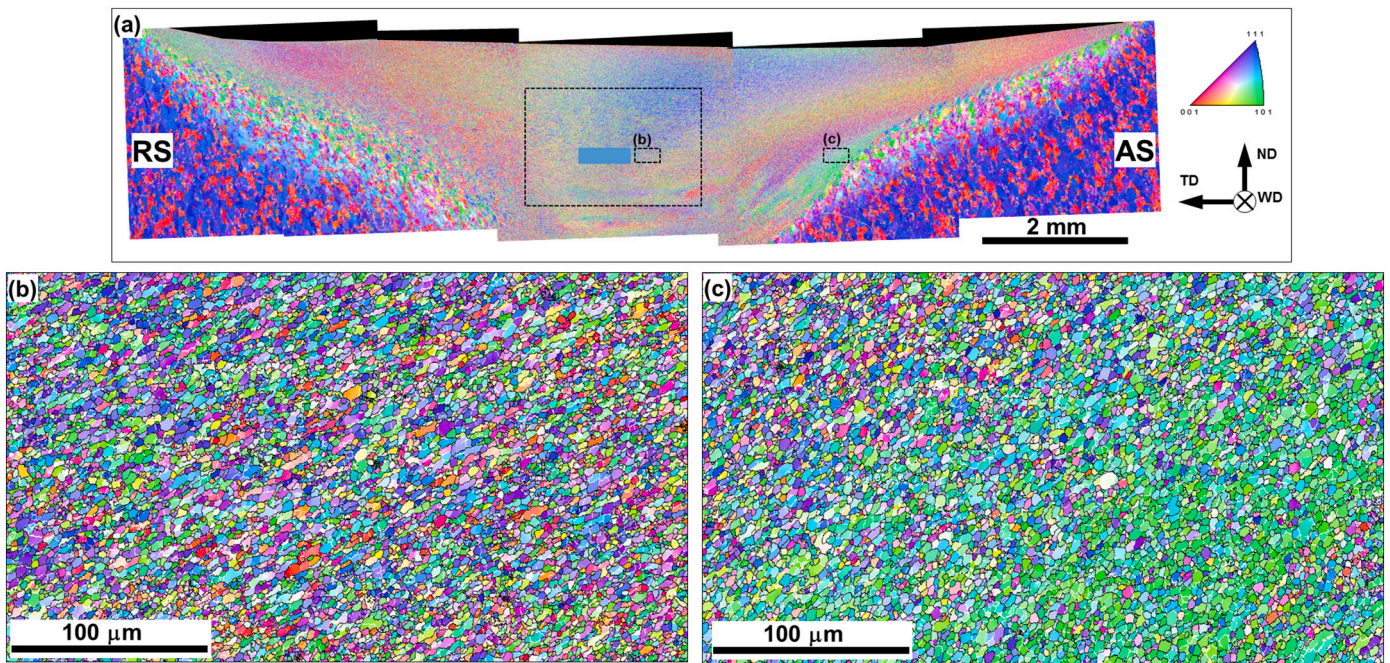
---

[4] In addition to FSW heat input, particle coarsening and dissolution were also obviously influenced by the large plastic deformation within the stir zone. However, the specific contributions of these mechanisms to particle behavior are unknown.

Fig. 5. (a) Sample-scale EBSD inverse-pole-figure (orientation) map taken from the low-heat-input weld with selected areas shown at higher magnification in (b) and (c). In the map, grains are colored according to their crystallographic orientations relative to the welding direction. (The color-code triangle is shown on the right side of (a)). In (b) and (c), LABs and HABs are depicted as white lines and black lines, respectively. Note: The large selected area in (a) indicates the microstructural region from which texture data were derived and shown in Fig. 14a. The aqua-colored rectangle shows the approximate location for SEM and TEM samples and the corresponding micrographs in Figs. 7a and 8a, respectively. (For interpretation of the references to color in this figure legend, the reader is referred to the web version of this article.)
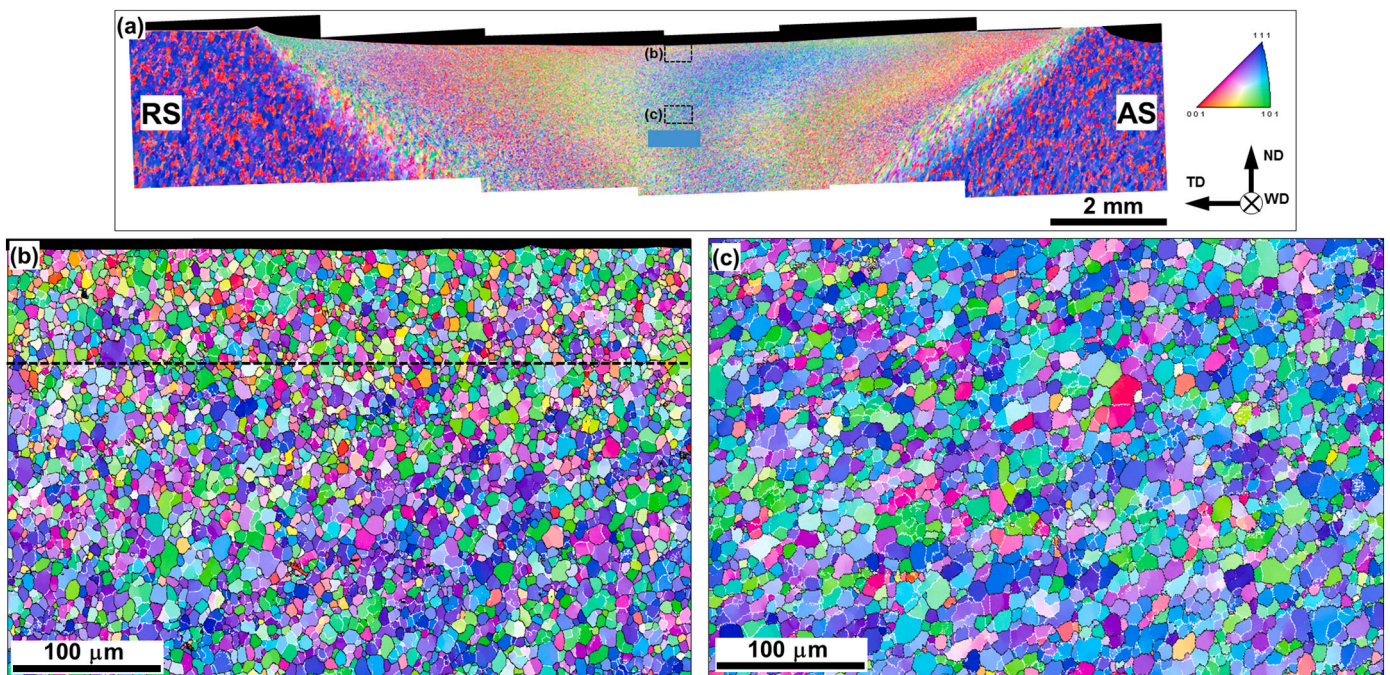

Fig. 6. (a) Sample-scale EBSD inverse-pole-figure (orientation) map taken from the high-heat-input weld with selected areas shown at higher magnification in (b) and (c). In the map, grains are colored according to their crystallographic orientations relative to the welding direction. (The color-code triangle is shown on the right side of (a)). In (b) and (c), LABs and HABs are depicted as white lines and black lines, respectively. In (b), the broken line approximates the surface layer. The aqua-colored rectangle shows the approximate location for SEM and TEM samples and the corresponding micrographs in Figs. 7b and 8b-c, respectively. (For interpretation of the references to color in this figure legend, the reader is referred to the web version of this article.)

4.3.1. Grain growth

4.3.1.1. Low-heat-input weld. In the *low-heat-input weld*, significant

microstructural coarsening was observed after heating to 450 °C (Fig. 10a). In almost the entire stir zone, a bimodal grain structure had developed in which comparatively fine (~15 μm) grains were

Table 2
Microstructural characteristics within the stir zone in the as-welded condition.

Material condition	Location within weld	Grain structure		Second-phase particles	
		Mean grain size (μm)	HAB fraction (%)	Volume fraction (%)	Mean diameter (nm)
Low-heat-input weld	Nugget	2.5	81	0.3	58
	AS	1.9	62	0.6	58
High-heat-input weld	Nugget	8.5	68	0.9	57
	Upper surface	3.1	58	1.0	58

intermixed with relatively coarse (~200 μm) ones (Fig. 11a). This bimodal nature suggested a clear difference in grain-growth kinetics and thus clear evidence of the abnormal character of this process.

A distinctly different microstructure was found at the AS of the stir zone (Fig. 11b). In this case, the FSW-induced microstructure remained largely unchanged except for a few grains which had experienced catastrophic coarsening, thus giving rise to the classical pattern of AGG. A comparison of Fig. 11b and a seemed to suggest that the number density of the growing grains on the AS was relatively low, and thus the AGG in this area was most pronounced.

A further increase of the heating temperature to 500 °C or 540 °C led to only minor microstructure changes (Figs. 10b and c), which in fact consisted only of the elimination of the original fine-grain microstructure on the AS.

4.3.1.2. High-heat-input weld. The *high-heat-input weld* exhibited noticeably-different annealing behavior (Fig. 12). In this case, the first evidence of microstructural coarsening was revealed only after heating to 500 °C (Fig. 12a), i.e., this welding condition showed superior thermal stability. Moreover, grain growth occurred only locally in the near-surface layer of the weld, whereas the microstructure of the remainder of the stir zone remained stable (Fig. 12a). Importantly, microstructural coarsening in the near-surface layer involved an abrupt coarsening of a few grains (Fig. 11c), thus being grossly abnormal. The preferential nucleation of the abnormal grains near the upper surface of the stir zone has been reported a number of times in the past [2–6,8,10,13,20,21,23,24,28].

It is important to emphasize that the microstructure developed in the central section of the stir zone during welding (i.e., the weld nugget) was very stable (Fig. 12c). High-resolution EBSD measurements showed that this microstructure experienced changes neither in morphology nor grain size (Fig. 11d). Therefore, it was eventually consumed by the abnormal grains propagating from the upper and bottom sections of the stir zone.

It is noteworthy that AGG in relatively-thick welds is often dominated by grains growing not from the upper surface but rather from the weld bottom [2–4,16]. This effect is usually attributed to the inhomogeneous microstructure distribution across the thickness of such welds [2,16].

4.3.2. Evolution of secondary particles

Statistical analysis showed that the secondary particles experienced only minor changes in volume fraction and size as the temperature was
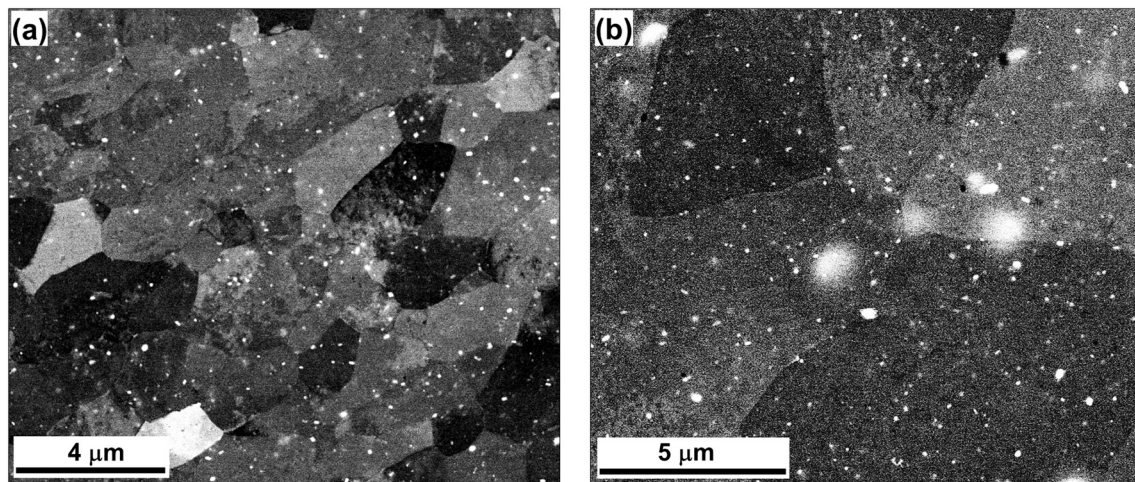

Fig. 7. Typical backscatter-electron scanning-electron-microscopy (BSE-SEM) images of the microstructure produced in the nugget of (a) the low-heat-input weld and (b) the high-heat-input weld. Note: Secondary particles appear bright in the images.
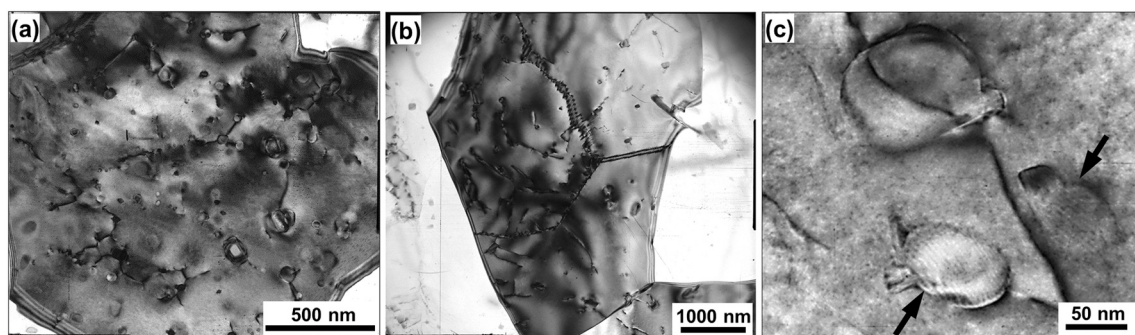

Fig. 8. Typical TEM images of the microstructure developed in the nugget of (a) the low-heat-input weld, and (b, c) the high-heat-input weld. In (c), the arrows indicate semi-coherent particles.
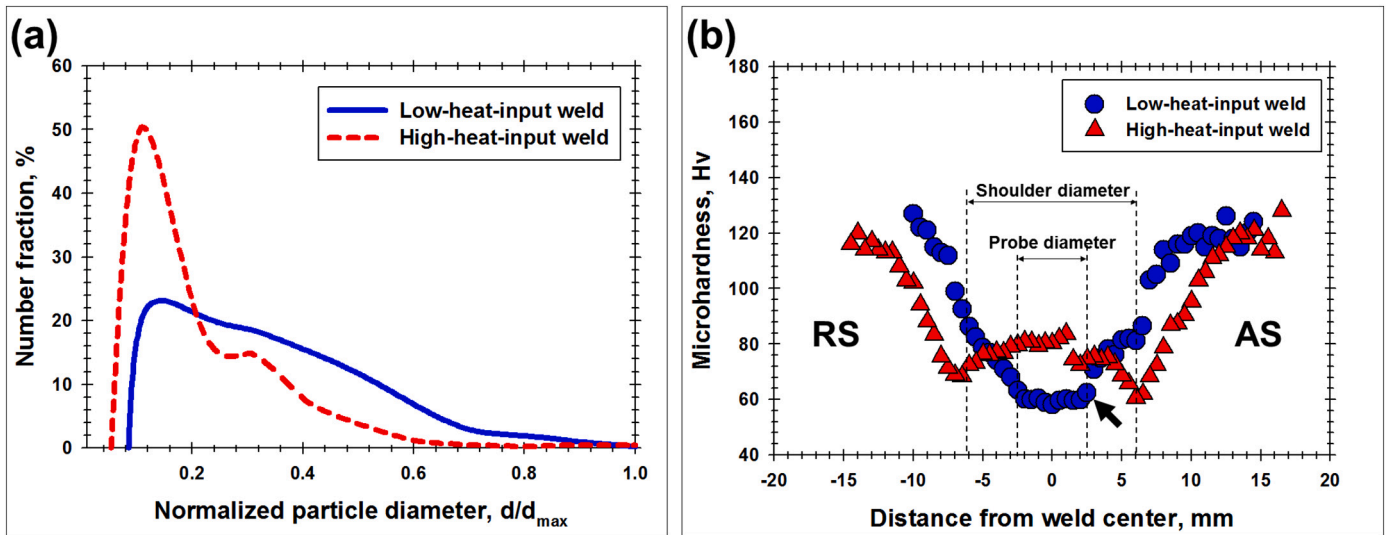
Fig. 9. Effect of welding condition on (a) the particle-size distribution in the weld nugget and (b) the microhardness profile measured across the width of the weld.
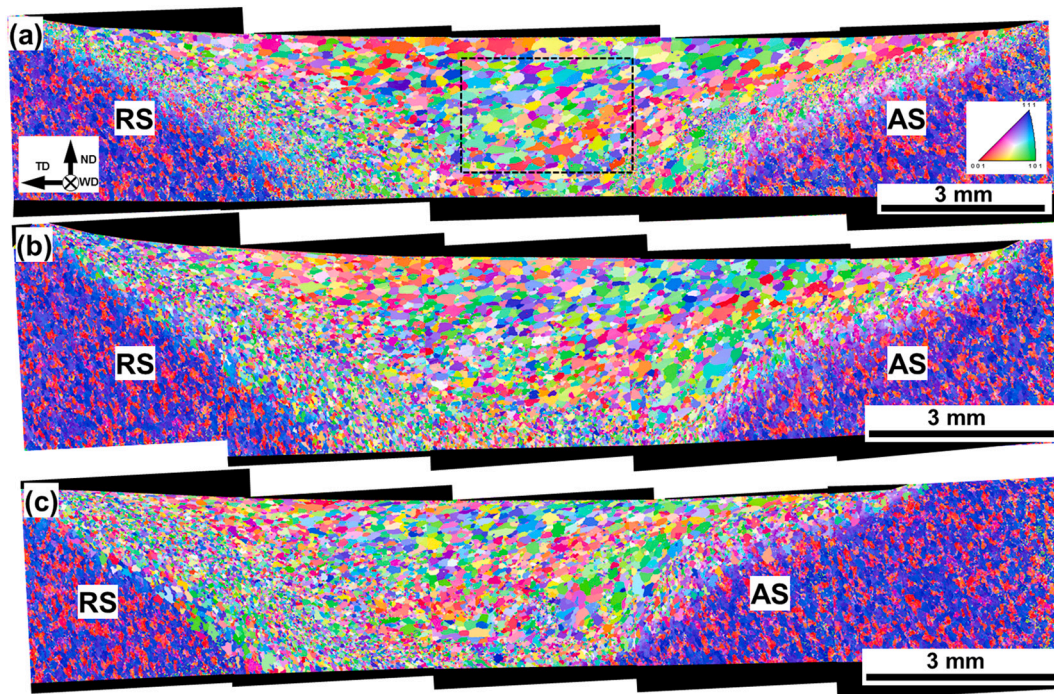

Fig. 10. Sample-scale EBSD inverse-pole-figure (orientation) maps taken from the low-heat-input weld after heating to (a) 450 °C, (b) 500 °C, and (c) 540 °C. In the maps, grains are colored according to their crystallographic orientations relative to the welding direction. (The color-code triangle is shown on the right side of (a)). After Kalinenko, et al. [57]. Note: The selected area in (a) indicates the microstructural region from which texture data were derived and shown in Fig. 14b.

increased during annealing (Figs. 13a and b). The sole exception was the nugget zone of the low-heat-input weld, in which a gradual *increase* in particle content was found (Fig. 13a). This effect was coupled with a marked increase in the number fraction of relatively-fine particles in the particle-size distribution (Fig. 13c). Taken together, these observations suggested a re-precipitation of the particles that dissolved during FSW according to ThermoCalc predictions (Fig. 4b).

There was also substantial scatter in the particle measurements (Fig. 13a). Considering the significant number of particles that were observed and associated reliability of the statistics (>1000 particles for each material condition), it was suggested that the scatter arose from a non-uniform distribution of particles due to the heterogeneous character of the re-precipitation process.

5. Discussion

5.1. Analysis in terms of Humphreys' cellular model

As pointed out in Section 1, the thermal stability of friction-stir welded materials is typically analyzed in terms of Humphreys' theory of the stability and growth of cellular structures [51,52]. According to this model, the annealing behavior of a particle-containing material is governed by the relationship between the mean grain radius R, the particle volume fraction F_v, and the mean particle size d; this relationship is expressed by the dimensionless parameter $Z = \frac{3F_v R}{d}$ [52]. Depending on the magnitude of Z, annealing behavior may vary widely, as summarized in Table 3.
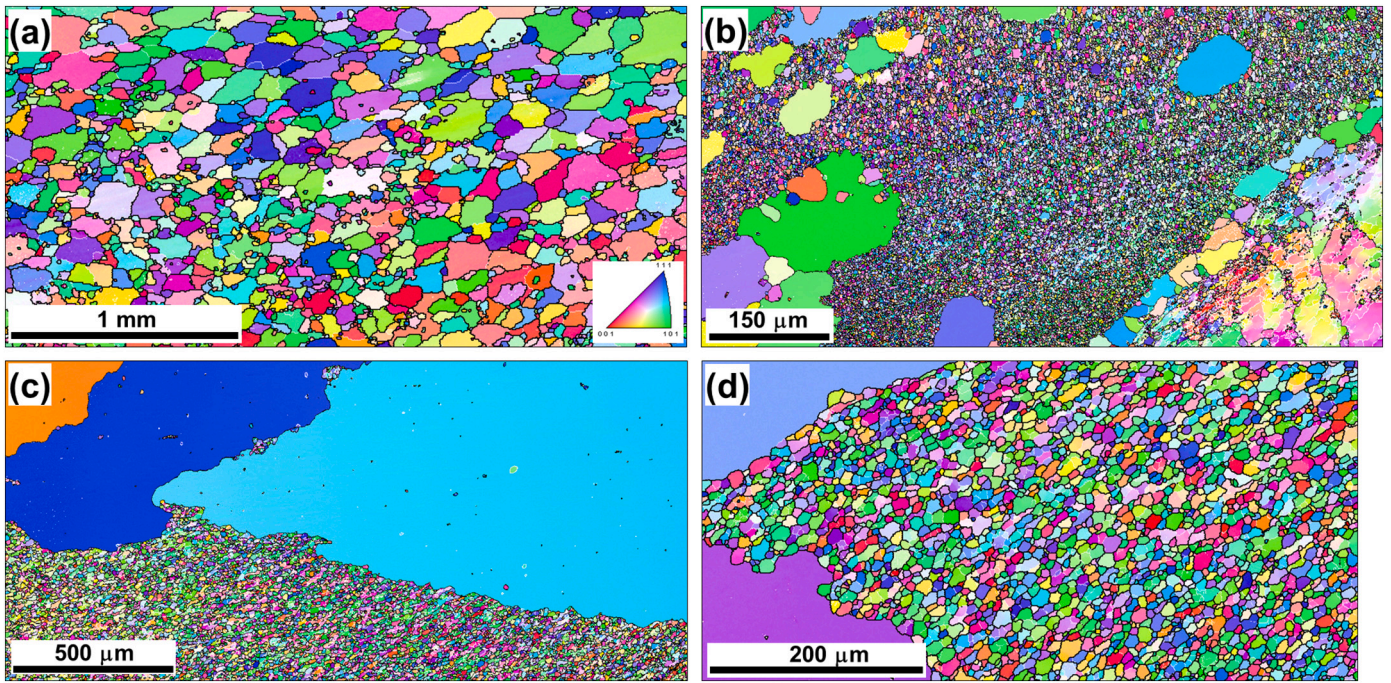
Fig. 11. High-resolution EBSD inverse-pole-figure maps showing microstructures developed in particular locations of the stir zone after different heating conditions: (a) low-heat-input weld, heated to 450 °C, nugget zone, (b) low-heat-input weld, heated to 450 °C, advancing side, (c) high-heat-input weld, heated to 525 °C, upper surface, (d) high-heat-input weld, heated to 540 °C, surviving fine-grain microstructure in the nugget zone. In all cases, individual grains in the maps are colored according to their crystallographic orientations relative to the welding direction. (The color-code triangle is shown in the bottom right corner of (a); LABs and HABs are depicted as white lines and black lines, respectively). Note difference in scales.
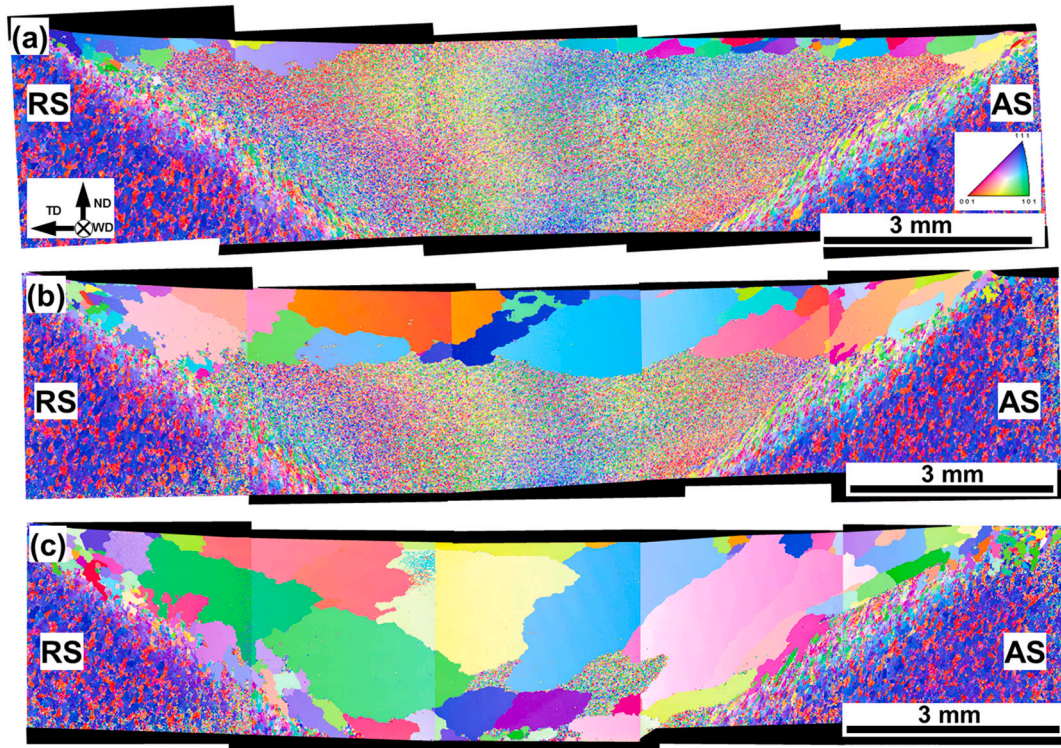

Fig. 12. Sample-scale EBSD inverse-pole-figure (orientation) maps taken from the high-heat-input weld after heating to (a) 500 °C, (b) 525 °C, or (c) 540 °C. In the maps, grains are colored according to their crystallographic orientations relative to welding direction. (The color-code triangle is shown on the right side of (a)). After Kalinenko, et al. [57].
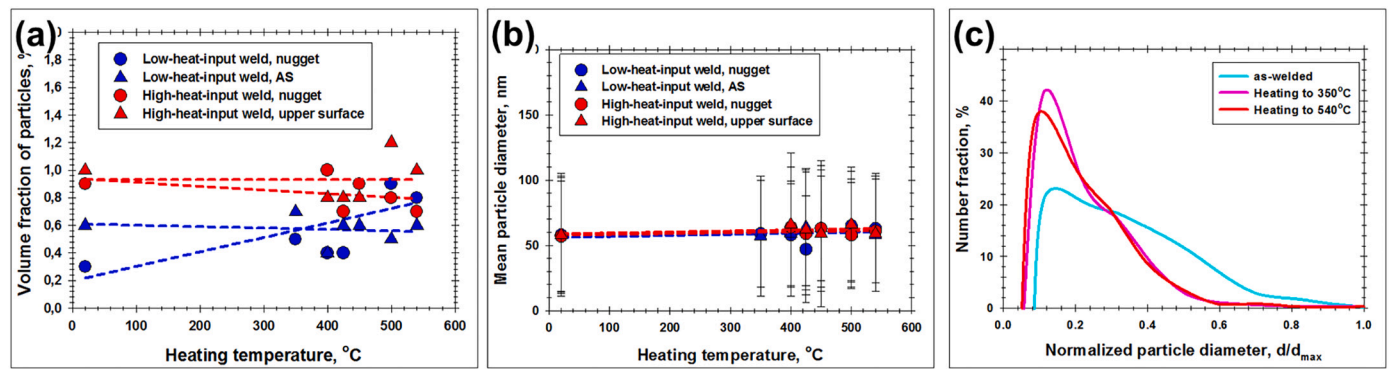
Fig. 13. Effect of heating temperature on characteristics of second-phase particles: (a) Volume fraction, (b) mean size, and (c) the particle-size distribution in the nugget of the low-heat-input weld.

Table 3

Characteristic annealing behaviors per Humphreys' cellular-growth model [52].

Parameter Z	Predicted annealing behavior
Z = 0	Normal grain growth
0 < Z < 0.1	Broadening of grain-size distribution
0.1 < Z < 0.25	Normal grain growth and abnormal grain growth
0.25 < Z < 1.0	Abnormal grain growth
Z > 1.0	No grain growth. Microstructure stability

Based on the experimental measurements/calculations of the Z parameter, expected annealing behaviors for both welded materials were predicted as a function of heating temperature. In both cases, the calculated values of Z varied over a wide range due to uncertainties in the particle measurements. Nevertheless, several important conclusions were drawn from these estimates and are summarized in the following two sections.

5.1.1. Low-heat-input weld

In the *nugget zone* of the low-heat-input weld, a combination of normal grain growth and AGG was predicted based on the Z values (Table 4). Generally, such a conclusion was consistent with the corresponding microstructure observations (Fig. 11a). Per Humphrey's theory, this annealing behavior may be attributed to the relatively-fine grain size and low concentration of secondary particles that resulted from the low-heat-input FSW (Table 4). Specifically, the low welding temperature provided grain refinement, whereas the high cooling rate

(Fig. 2) prevented re-precipitation of dissolved particles during the weld cooling cycle. The comparatively high HAB fraction associated with this welding condition was another factor that may have promoted activation of normal grain growth (Table 2).

On the AS of the stir zone, the presumed wear of the welding tool provided an increase in the particle volume fraction (Table 2). Considering the relatively-fine grain size, however, this effect was not sufficient for complete microstructural stabilization. In contrast, it shifted annealing behavior into an entirely AGG range (Table 4, Fig. 11b).

5.1.2. High-heat-input weld

Based on calculated values of Z, the microstructure produced in the *weld nugget* of the high-heat-input weld was predicted to be stable against AGG (Table 5). This result was in excellent agreement with the observed material behavior (Fig. 12). According to Humphrey's model, such microstructure stability was associated with the comparatively-large grain size and the high particle content revealed in the high-heat-input weld (Table 2). In particular, the elevated FSW temperature provided a coarse-grain structure, whereas the low cooling rate enabled partial re-precipitation of dissolved particles after FSW (Fig. 2).

In this welding condition, however, annealing behavior within the stir-zone material was greatly influenced by the *near-surface layer* associated with the tool shoulder. Due to the relatively fine-grained microstructure with a high concentration of secondary particles (Table 2), material in this layer was prone to AGG (Table 5, Fig. 11c). The abnormal grains that evolved in this region grew catastrophically, thus consuming the nominally-stable microstructure of the remaining

Table 4

Analysis of the annealing behavior of the low-heat-input weld in terms of Humphreys' cellular-growth model.

Annealing condition	Particle volume fraction (F_v)	Particle mean diameter, d (μm)	$\frac{F_v}{d}$ (μm^{-1})	Mean grain radius, R (μm)	$Z = \frac{3F_vR}{d}$	Predicted annealing behavior
Nugget						
As-welded condition	0.003	0.058	0.052	1.3	0.20	
Heating to 350 °C	0.005	0.059	0.085	1.3	0.33	Normal grain growth + abnormal grain growth
Heating to 400 °C	0.004	0.058	0.069	1.3	0.27	
Heating to 425 °C	0.004	0.047	0.085	1.3	0.33	
Heating to 450 °C	0.009	0.063	0.143	≈50	21.43	
Heating to 500 °C	0.009	0.065	0.138	≈50	20.77	No grain growth
Heating to 540 °C	0.008	0.063	0.127	≈50	19.05	
Advancing side						
As-welded condition	0.006	0.058	0.103	1.0	0.31	
Heating to 350 °C	0.007	0.057	0.123	1.0	0.37	Abnormal grain growth
Heating to 400 °C	0.004	0.059	0.068	1.0	0.20	
Heating to 425 °C	0.006	0.064	0.094	1.0	0.28	
Heating to 450 °C	0.006	0.063	0.095	1.0	0.29	
Heating to 500 °C	0.005	0.059	0.085	≈50	12.71	No grain growth
Heating to 540 °C	0.006	0.058	0.103	≈50	15.52	

Table 5

Analysis of the heating behavior of the high-heat-input weld in terms of Humphreys' cellular-growth model.

Annealing condition	Particle volume fraction (F_v)	Particle mean diameter, d (μm)	$\frac{F_v}{d}$ (μm^{-1})	Mean grain radius R (μm)	$Z = \frac{3F_vR}{d}$	Predicted annealing behavior
Nugget						
As-welded condition	0.009	0.057	0.158	4.3	2.04	
Heating to 400 °C	0.010	0.064	0.156	4.3	2.02	
Heating to 425 °C	0.007	0.059	0.119	4.3	1.53	No grain growth
Heating to 450 °C	0.009	0.063	0.143	4.3	1.84	
Heating to 500 °C	0.008	0.058	0.138	4.3	1.78	
Heating to 540 °C	0.007	0.061	0.115	4.3	1.48	
Upper surface						
As-welded condition	0.010	0.058	0.172	1.6	0.83	
Heating to 400 °C	0.008	0.066	0.121	1.6	0.58	Abnormal grain growth
Heating to 425 °C	0.008	0.062	0.129	1.6	0.62	
Heating to 450 °C	0.008	0.059	0.136	≈50	20.34	
Heating to 500 °C	0.012	0.066	0.182	≈50	27.27	No grain growth
Heating to 540 °C	0.010	0.059	0.169	≈50	25.42	

stir zone (Fig. 12). This finally resulted in millimeter-scale grains (Fig. 12).

5.1.3. Relationship between microstructure and annealing behavior

From the above considerations, it follows that the post-weld annealing behavior of the stir zone material was closely linked with the particular FSW conditions. In low-heat-input welds, a combination of comparatively-fine grain size, high HAB fraction, and low particle content gave rise to a competition between normal grain growth and AGG. As a result, the final grain size was relatively small. Thus, in agreement with the recent work by Zuiko et al. [56], the lowering of FSW heat input promoted an inhibition of AGG. However, this undesirable effect was not suppressed *completely* (Figs. 11a, b). According to Humphreys' theory, this effect would be expected for Z < 0.1 (Table 3), which is perhaps achievable only for specific FSW conditions.

In the high-heat-input condition, in contrast, the relatively-coarse grain size and high particle fraction in the weld nugget provided microstructural stability. In such welds, however, an inhomogeneous microstructure distribution may develop across the stir zone thickness, which may trigger AGG. The abnormal grains which nucleate at the upper weld surface can then grow catastrophically to a millimeter-scale, thus consuming the rest of the stir zone.

5.2. Influence of grain-boundary mobility on AGG

In order to provide additional insight into the AGG phenomenon, the crystallographic orientations of the abnormal grains were measured. Due to the extremely limited statistics for the abnormal grains in the high-heat-input weld (Fig. 12), texture analysis was limited to the low-heat-input condition only. In particular, attention was focused on 111 and 110 pole figures (Figs. 14a and b, respectively) derived from EBSD data taken from the weld nugget in the as-FSW'ed. condition (Fig. 5a) as well as that after post-weld heating to 450 °C (Fig. 10a). The corresponding orientation distribution functions are given in supplementary Fig. S11. For comparative purposes, the ideal simple-shear orientations expected for face-centered cubic metals are given in Fig. 14c.[5]

In the as-welded state, the texture was dominated by an {*hkl*} < 110> fiber with a pronounced $B/\overline{B}\{112\}\langle110\rangle$ component (compare Figs. 14a and c). Such textures are typically found in the stir zone of aluminum alloys [76]. Importantly, the texture in Fig. 14a suggested a proximity of the shear plane to the shoulder surface (compare Figs. 14a and c), thus indicating a significant contribution of the tool shoulder to global material flow. This effect was likely due to the relatively-small

thickness of the welded sheets (i.e., 3 mm).

AGG that occurred during the heating of the welded sample to 450 °C resulted in significant texture changes (compare Figs. 14a and b). To a first approximation, this transformation could be described as a ~ 40° rotation of the FSW-induced texture around a < 111> axis.[6] A similar effect has been reported in previous work [75]. On the other hand, a 25-35° ⟨110⟩ rotation of the original texture during abnormal grain growth has been reported in Ref. [50].

In the theory of *recrystallization* textures, such crystallographic reorientation is well known, and is usually explained in terms of two competing mechanisms, viz., oriented nucleation and/or oriented growth [77]. According to the first possibility, texture changes result from the preferential development of recrystallization nuclei of particular crystallographic orientations and associated variations in stored dislocation density (i.e., stored energy) from grain to grain. On the other hand, the oriented-growth concept is based on the enhanced mobility of 40° < 111> boundaries in cubic metals.

In the present work, the stir-zone material in both welded conditions had a *low* dislocation density (Figs. 8a and b), presumably due to continuous dynamic recrystallization during FSW. Therefore, it is unlikely that the texture rotation during subsequent annealing (and AGG) can be explained in terms of the oriented-nucleation model. In particular, the area fraction of 40° < 111> boundaries in the as-FSPed condition was typically below 0.5% (a typical example is shown in supplementary Figs. S12a and b). In the microstructure, however, such boundaries were often observed between grains belonging to the dominant texture component (i.e., {hkl}⟨110⟩ fiber) and grains having other crystallographic orientations (supplementary Figs. S12c). From the broad perspective, therefore, the preferential migration of 40°⟨111⟩ boundaries might indeed promote the selective character of grain growth and simultaneously rotate the crystallographic texture by 40° around a < 111> axis. On the other hand, it is important to emphasize that no direct evidence of an increased mobility of 40°<111 > boundaries was actually observed in the present study, and thus the relevance of the above mechanism warrants experimental verification.

In summary, AGG in the present work appears to be governed by at least two factors, i.e., the pinning effect exerted by secondary particles on grain boundaries and (possibly) the enhanced mobility of 40° < 111> boundaries. The exact contribution of each mechanism (as well as their interrelation) warrants further investigation, however.

---

[5] Note: The pole figures aligned with the local shear frame are shown in supplementary Fig. S10.

[6] To illustrate the texture rotation, red dotted lines were superimposed on the 111 pole figures in Figs. 14a, b.
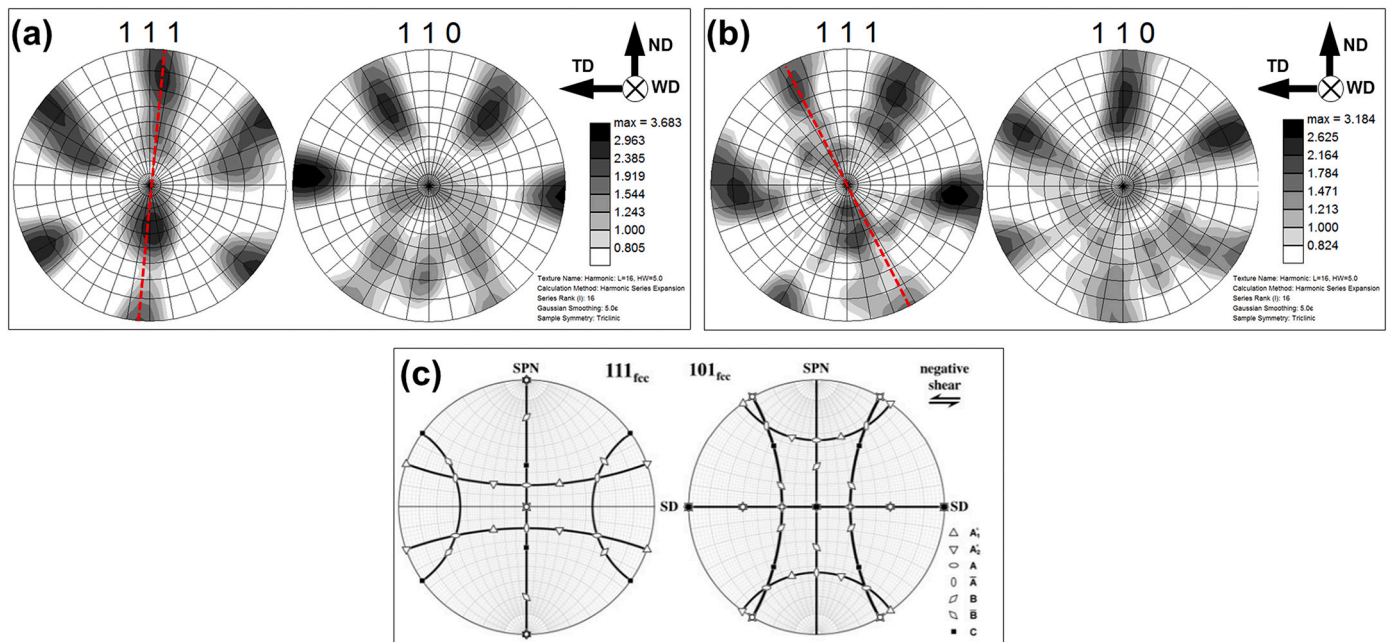
Fig. 14. Effect of microstructural coarsening in low-heat-input weld on crystallographic texture: 111 and 110 pole figures taken from the weld nugget (a) in the as-welded condition, (b) after heating to 450 °C and the concomitant grain growth, and (c) the ideal simple-shear textures expected for face-centered cubic crystals (after Fonda et al. [75]). SD, and SPN are shear direction, and shear plane normal, respectively. In (a) and (b), red lines illustrate ~40° ⟨111⟩ rotation of the texture during microstructural coarsening. See Section 5.2 for details. (For interpretation of the references to color in this figure legend, the reader is referred to the web version of this article.)

6. Conclusions

FSW of aluminum alloy 6061-T6 was performed to shed light on the phenomenon of AGG in heat-treatable aluminum alloys. To this end, the relationship between the weld heat input, the FSW-induced microstructure, and subsequent annealing behavior was investigated. Particular attention was given to the microstructural processes occurring at the early stage of the post-weld heat treatment. The main conclusions derived from this work are as follows.

(1) FSW leads to complex precipitation phenomena in the stir zone, including coarsening, dissolution, and partial re-precipitation during the weld cooling cycle. In the *low-heat-input condition*, due to the relatively low welding temperature and high cooling rate, particle behavior is dominated by a particle-coarsening mechanism. In contrast, a combination of high FSW temperature and low cooling rate in the *high-heat-input condition* promotes re-precipitation of particles which have dissolved during the weld cooling cycle. As a result, the particle content in the high-heat-input weld is found to be higher than that in the low-heat-input one.

(2) Post-weld annealing behavior is closely linked with the FSW heat input. In the low-heat-input weld, a combination of comparatively-fine grain size, high HAB fraction, and low particle content result in a competition between normal grain growth and AGG. As a consequence, the final grain size is relatively small (~100 μm). In the high-heat-input condition, in contrast, the relatively-coarse grain size and high particle fraction in the weld nugget provide microstructural stabilization. However, the weak point of such welds comprises a fine-grain surface layer induced by the stirring action of the tool shoulder. The abnormal grains that evolve in this region grow catastrophically to a millimeter-scale, thus consuming the grains elsewhere in the stir zone. In both welded states, post-weld annealing behavior can be explained in terms of Humphrey's cellular-growth model.

(3) AGG develops at a very early stage of post-weld solution treatment. In fact, this process is nearly-completed during the heating stage of the treatment, i.e., during the heating from ambient conditions to the peak solution temperature.

(4) AGG is found to result in a 40°⟨111⟩ rotation of the crystallographic texture in the stir zone. This phenomenon is hypothesized on the basis of the oriented-growth theory. Hence, on the basis of experimental observations, two AGG mechanisms are suggested, viz., a pinning effect exerted by secondary particles and an enhanced mobility of 40°⟨111⟩ boundaries.

Declaration of Competing Interest

The authors declare that they have no known competing financial interests or personal relationships that could have appeared to influence the work reported in this paper.

Data availability

The raw/processed data required to reproduce these findings cannot be shared at this time due to technical or time limitations.

Appendix A. Supplementary data

Supplementary data to this article can be found online at https://doi.org/10.1016/j.matchar.2022.112473.

References

[1] R.S. Mishra, Z.Y. Ma, Friction stir welding and processing, Mater. Sci. Eng. R 50 (2005) 1–78, https://doi.org/10.1016/j.mser.2005.07.001.

[2] Kh.A.A. Hassan, A.F. Norman, D.A. Price, P.B. Prangnell, Stability of nugget zone grain structure in high strength Al-alloy friction stir welds during solution treatment, Acta Mater. 57 (2003) 1923–1936, https://doi.org/10.1016/S1359-6454(02)00598-0.

[3] I. Charit, R.S. Mishra, Abnormal grain growth in friction stir processed alloys, Scr. Mater. 58 (2008) 367–371, https://doi.org/10.1016/j.scriptamat.2007.09.052.

[4] F.C. Liu, Z.Y. Ma, L.Q. Chen, Low-temperature superplasticity of Al-mg-Sc alloy produced by friction stir processing, Scr. Mater. 60 (2009) 968–971, https://doi.org/10.1016/j.scriptamat.2009.02.021.

[5] S. Mironov, K. Masaki, Y.S. Sato, H. Kokawa, Relationship between material flow and abnormal grain growth in friction-stir welds, Scr. Mater. 67 (2012) 983–986, https://doi.org/10.1016/j.scriptamat.2012.09.002.

[6] M.M. Attallah, H.G. Salem, Friction stir welding parameters: a tool for controlling abnormal grain growth during subsequent heat treatment, Mater. Sci. Eng. A 391 (2005) 51–59, https://doi.org/10.1016/j.msea.2004.08.059.

[7] F.C. Liu, B.L. Xiao, K. Wang, Z.Y. Ma, Investigation of superplasticity in friction stir processed 2219 Al alloy, Mater. Sci. Eng. A 527 (2010) 4191–4196, https://doi.org/10.1016/j.msea.2010.03.065.

[8] M.A. Garcia-Bernal, R.S. Mishra, R. Verma, D. Hernandez-Silva, Inhibition of abnormal grain growth during hot deformation of friction stir processed 5083 Al alloys, Mater. Sci. Eng. A 636 (2015) 326–330, https://doi.org/10.1016/j.msea.2015.03.094.

[9] S. Malopheyev, S. Mironov, I. Vysotskiy, R. Kaibyshev, Superplasticity of friction-stir welded Al-mg-Sc sheets with ultrafine-grained microstructure, Mater. Sci. Eng. A 649 (2016) 85–92, https://doi.org/10.1016/j.msea.2015.09.106.

[10] Y. Chen, H. Ding, J. Li, Z. Cai, J. Zhao, W. Yang, Influence of multi-pass friction stir processing on the microstructure and mechanical properties of Al-5083 alloy, Mater. Sci. Eng. A 650 (2016) 281–289, https://doi.org/10.1016/j.msea.2015.10.057.

[11] M.A. Garcia-Bernal, R.S. Mishra, R. Verma, D. Hernandez-Silva, Influence of friction stir processing tool design on microstructure and superplastic behavior of Al-mg alloys, Mater. Sci. Eng. A 670 (2016) 9–16, https://doi.org/10.1016/j.msea.2016.05.115.

[12] I. Vysotskiy, S. Malopheyev, S. Mironov, R. Kaibyshev, Pre-strain rolling as an effective tool for suppression of abnormal grain growth in friction-stir welded 6061 aluminum alloy, Mater. Sci. Eng. A 733 (2018) 39–42, https://doi.org/10.1016/j.msea.2018.07.026.

[13] Q. Pang, J.H. Zhang, M.J. Huq, Z.L. Hu, Characterization of microstructure, mechanical properties and formability for thermomechanical treatment of friction stir welded 2024-O alloys, Mater. Sci. Eng. A 765 (2019), 138303, https://doi.org/10.1016/j.msea.2019.138303.

[14] I. Vysotskiy, S. Malopheyev, S. Mironov, R. Kaibyshev, Effect of pre-strain path on suppression of abnormal grain growth in friction-stir welded 6061 aluminum alloy, Mater. Sci. Eng. A 760 (2019) 206–213, https://doi.org/10.1016/j.msea.2019.05.118.

[15] P. Nelaturu, S. Jana, R.S. Mishra, G. Grant, B.E. Carlson, Effect of temperature on the fatigue cracking mechanisms in A356 Al alloy, Mater. Sci. Eng. A 780 (2020), 139175, https://doi.org/10.1016/j.msea.2020.139175.

[16] M.B. Lezaack, A. Simar, Avoiding abnormal grain growth in thick 7XXX aluminium alloy friction stir welds during T6 post heat treatments, Mater. Sci. Eng. A 807 (2021), 140901, https://doi.org/10.1016/j.msea.2021.140901.

[17] N. Kumar, R.S. Mishra, Thermal stability of friction stir processed ultrafine grained AlMgSc alloy, Mater. Charact. 74 (2012) 1–10, https://doi.org/10.1016/j.matchar.2012.09.003.

[18] Z.L. Hu, X.S. Wang, Q. Pang, F. Huang, X.P. Qin, L. Hua, The effect of postprocessing on tensile property and microstructure evolution of friction stir welding aluminum alloy joint, Mater. Charact. 99 (2015) 180–187, https://doi.org/10.1016/j.matchar.2014.11.015.

[19] Y.S. Sato, H. Watanabe, H. Kokawa, Grain growth phenomena in friction stir welded 1100 Al during post-weld heat treatment, Sci. Technol. Weld. Join. 12 (2007) 318–323, https://doi.org/10.1179/174329307X197575.

[20] K. Chen, W. Gan, K. Okamoto, C. Kwansoo, R.H. Wagoner, The mechanism of grain coarsening in friction-stir-welded AA5083 after heat treatment, Metal. Mater. Trans. A 42 (2011) 488–507, https://doi.org/10.1007/s11661-010-0426-9.

[21] S. Mironov, K. Masaki, Y.S. Sato, H. Kokawa, Texture produced by abnormal grain growth in friction stir-welded aluminum alloy 1050, Metal. Mater. Trans. A 44 (2013) 1153–1157, https://doi.org/10.1007/s11661-012-1596-4.

[22] G. Ipekoglu, S. Erim, G. Cam, Investigation into the influence of post-weld heat treatment on the friction stir welded AA6061Al-alloy plates with different temper conditions, Metal. Mater. Trans. A 45 (2014) 864–877, https://doi.org/10.1007/s11661-013-2026-y.

[23] S. Mironov, Y. Motohashi, R. Kaibyshev, Grain growth behavior in a friction-stir welded ZK60 magnesium alloy, Mater. Trans. 48 (2007) 1387–1395, https://doi.org/10.2320/matertrans.MRA2007040.

[24] H. Yoshioka, S. Fukumoto, A. Yamamoto, H. Tsubakino, K. Okita, T. Tomita, Effect of post weld heat treatment on mechanical properties and microstructures of friction stir welded AZ31B magnesium alloy, J. Jap. Inst. Light Metal 58 (2008) 2–7, https://doi.org/10.2464/jilm.58.2.

[25] M. Mosayebi, A. Zarei-Hanzaki, H.R. Abedi, A. Barabi, M.S. Jalali, A. Ghaderi, M. Barnett, The correlation between the recrystallization texture and subsequent isothermal grain growth in a friction stir processed rare earth containing magnesium alloy, Mater. Charact. 163 (2020) 110236, https://doi.org/10.1016/j.matchar.2020.110236.

[26] Y. Sun, H. Fujii, Effect of abnormal grain growth on microstructure and mechanical properties of friction stir welded SPCC steel plates, Mater. Sci. Eng. A 694 (2017) 81–92, https://doi.org/10.1016/j.msea.2017.04.008.

[27] Y.J. Li, R.D. Fu, D.X. Du, L.J. Jing, D.L. Sang, Y.P. Wang, Effect of post-weld heat treatment on microstructures and properties of friction stir welded joint of 32Mn–7Cr–1Mo–0·3N steel, Sci. Technol. Weld. Join. 20 (2015) 229–235, https://doi.org/10.1179/1362171815Y.0000000001.

[28] H. Dawson, M. Serrano, S. Cater, E. Jimenez-Melero, Characterization of ODS steel friction stir welds and their abnormal grain growth behavior, Fusion Eng. Design 135 (2018) 174–182, https://doi.org/10.1016/j.fusengdes.2018.07.021.

[29] Y. Li, R. Fu, Y. Li, Y. Peng, H. Liu, Abnormal grain growth in the heat affected zone of friction stir welded joint of 32Mn-7Cr-1Mo-0.3N steel during post-weld heat treatment, Metal. 8 (2018) 254, https://doi.org/10.3390/met8040254.

[30] F. Khodabakhshi, A. Simchi, A.H. Kokabi, A.P. Gerlich, M. Nosko, Effects of post-annealing on the microstructure and mechanical properties of friction stir processed Al-Mg-TiO$_2$ nanocomposites, Mater. Design. 63 (2014) 30–41, https://doi.org/10.1016/j.matdes.2014.05.065.

[31] J. Guo, B.Y. Lee, Z. Du, B.G. Bi, M.J. Tan, J. Wei, Effect of nano-particle addition on grain structure evolution of friction stir-processed Al 6061 during postweld annealing, JOM 68 (2016) 2268–2273, https://doi.org/10.1007/s11837-016-1991-1.

[32] J.-Q. Su, T.W. Nelson, R. Mishra, M. Mahoney, Microstructural investigation of friction stir welded 7050-T651 aluminium, Acta Mater. 51 (2003) 713–729, https://doi.org/10.1016/S1359-6454(02)00449-4.

[33] C. Genevois, A. Deschamps, A. Denquin, B. Doisneau-cottignies, Quantitative investigation of precipitation and mechanical behaviour for AA2024 friction stir welds, Acta Mater. 53 (2005) 2447–2458, https://doi.org/10.1016/j.actamat.2005.02.007.

[34] M. Dumont, A. Steuwer, A. Deschamps, M. Peel, P.J. Withers, Microstructure mapping in friction stir welds of 7449 aluminium alloy using SAXS, Acta Mater. 54 (2006) 4793–4801, https://doi.org/10.1016/j.actamat.2006.06.015.

[35] A. Steuwer, M. Dumont, J. Altenkirch, S. Birosca, A. Deschamps, P.B. Prangnell, P. J. Withers, A combined approach to microstructure mapping of an Al–Li AA2199 friction stir weld, Acta Mater. 59 (2011) 3002–3011, https://doi.org/10.1016/j.actamat.2011.01.040.

[36] C.G. Rhodes, M.W. Mahoney, W.H. Bingel, R.A. Spurling, C.C. Bampton, Effects of friction stir welding on microstructure of 7075 aluminium, Scr. Mater. 36 (1997) 69–75, https://doi.org/10.1016/S1359-6462(96)00344-2.

[37] M.J. Jones, P. Heurtier, C. Desrayaud, F. Montheillet, D. Allehaux, J.H. Driver, Correlation between microstructure and microhardness in a friction stir welded 2024 aluminium alloy, Scr. Mater. 52 (2005) 693–697, https://doi.org/10.1016/j.scriptamat.2004.12.027.

[38] C.A.W. Olea, L. Roldo, J.F. dos Santos, T.R. Strohaecker, A sub-structural analysis of friction stir welded joints in an AA6056 Al-alloy in T4 and T6 temper conditions, Mater. Sci. Eng. A 454–455 (2007) 52–62, https://doi.org/10.1016/j.msea.2006.12.055.

[39] A. Simar, Y. Bréchet, B. de Meester, A. Denquin, T. Pardoen, Microstructure, local and global mechanical properties of friction stir welds in aluminium alloy 6005A-T6, Mater. Sci. Eng. A 486 (2008) 85–95, https://doi.org/10.1016/j.msea.2007.08.041.

[40] P. Dong, D. Sun, H. Li, Natural aging behaviour of friction stir welded 6005A-T6 aluminium alloy, Mater. Sci. Eng. A 576 (2013) 29–35, https://doi.org/10.1016/j.msea.2013.03.077.

[41] H. Qin, H. Zhang, H. Wu, The evolution of precipitation and microstructure in friction stir welded 2195-T8 Al–Li alloy, Mater. Sci. Eng. A 626 (2015) 322–329, https://doi.org/10.1016/j.msea.2014.12.026.

[42] P. Bala Srinivasan, K.S. Arora, W. Dietzel, S. Pandey, M.K. Schaper, Characterisation of microstructure, mechanical properties and corrosion behaviour of an AA2219 friction stir weldment, J. Al. Compd. 492 (2010) 631–637, https://doi.org/10.1016/j.jallcom.2009.11.198.

[43] B. Cai, Z.Q. Zheng, D.Q. He, S.C. Li, H.P. Li, Friction stir weld of 2060 Al–cu–Li alloy: microstructure and mechanical properties, J. Al. Compd. 649 (2015) 19–27, https://doi.org/10.1016/j.jallcom.2015.02.124.

[44] Y.S. Sato, H. Kokawa, M. Enomoto, S. Jogan, Microstructural evolution of 6063 aluminum during friction-stir welding, Metall. Mater. Trans. A 30 (1999) 2429–2437, https://doi.org/10.1007/s11661-999-0251-1.

[45] K.V. Jata, K.K. Sankaran, J.J. Ruschau, Friction-stir welding effects on microstructure and fatigue of aluminum alloy 7050-T7451, Metall. Mater. Trans. A 31 (2000) 2181–2192, https://doi.org/10.1007/s11661-000-0136-9.

[46] B. Heinz, B. Skrotzki, Characterization of a friction-stir-welded aluminum alloy 6013, Metall. Mater. Trans. B Process Metall. Process. Sci. 33 (2002) 489–498, https://doi.org/10.1007/s11663-002-0059-5.

[47] R.W. Fonda, J.F. Bingert, Precipitation and grain refinement in a 2195 Al friction stir weld, Metall. Mater. Trans. A 37 (2006) 3593–3604, https://doi.org/10.1007/s11661-006-1054-2.

[48] W. Woo, H. Choo, D.W. Brown, Z. Feng, Influence of the tool pin and shoulder on microstructure and natural aging kinetics in a friction-stir-processed 6061–T6 aluminum alloy, Metall. Mater. Trans. A 38 (2007) 69–76, https://doi.org/10.1007/s11661-006-9034-0.

[49] T.L. Giles, K. Oh-Ishi, A.P. Zhilyaev, S. Swaminathan, M.W. Mahoney, T. R. McNelley, The effect of friction stir processing on the microstructure and mechanical properties of an aluminum lithium alloy, Metall. Mater. Trans. A 40 (2009) 104–115, https://doi.org/10.1007/s11661-008-9698-8.

[50] A. Kalinenko, I. Vysotskii, S. Malopheyev, S. Mironov, R. Kaibyshev, Relationship between welding conditions, abnormal grain growth and mechanical performance in friction-stir welded 6061-T6 aluminum alloy, Mater. Sci. Eng. A 817 (2021), 141409, https://doi.org/10.1016/j.msea.2021.141409.

[51] F.J. Humphreys, A unified theory of recovery, recrystallization and grain growth, based on the stability and growth of cellular microstructures—I. the basic model, Acta Mater. 45 (1997) 4231–4240, https://doi.org/10.1016/S1359-6454(97)00070-0.

[52] F.J. Humphreys, A unified theory of recovery, recrystallization and grain growth, based on the stability and growth of cellular microstructures—II. The effect of second-phase particles, Acta Mater. 45 (1997) 5031–5039, https://doi.org/10.1016/S1359-6454(97)00173-0.

[53] S. Mironov, K. Inagaki, Y.S. Sato, H. Kokawa, Effect of welding temperature on microstructure of friction-stir welded aluminum alloy 1050, Metal. Mater. Trans. A 46 (2015) 783–790, https://doi.org/10.1007/s11221-014-2651-0.

[54] A. Kalinenko, K. Kim, I. Vysotskiy, I. Zuiko, S. Malopheyev, S. Mironov, R. Kaibyshev, Microstructure-strength relationship in friction-stir welded 6061-T6 aluminum alloy, Mater. Sci. Eng. A 793 (2020), 139858, https://doi.org/10.1016/j.msea.2020.139858.

[55] I.S. Zuiko, S. Mironov, R. Kaibyshev, Unusual ageing behaviour of friction-stir welded Al–cu–mg alloy, Mater. Sci. Eng. A 793 (2020), 139882, https://doi.org/10.1016/j.msea.2020.139882.

[56] I.S. Zuiko, S. Mironov, S. Betsofen, R. Kaibyshev, Suppression of abnormal grain growth in friction-stir welded Al–Cu–Mg alloy by lowering of welding temperature, Scr. Mater. 196 (2021), 113765, https://doi.org/10.1016/j.scriptamat.2021.113765.

[57] A. Kalinenko, I. Vysotskiy, S. Malopheyev, S. Mironov, R. Kaibyshev, New insight into the phenomenon of the abnormal grain growth in friction-stir welded aluminum, Mater. Lett. 302 (2021), 130407, https://doi.org/10.1016/j.matlet.2021.130407.

[58] W.J. Arbegast, Hot deformation of aluminum alloys III, in: TMS Annual Meeting, CA, San Diego, 2003, p. 313.

[59] F.J. Humphreys, Quantitative metallography by electron backscatter diffraction, J. Microsc. 195 (1999) 170–185, https://doi.org/10.1046/j.1365-2818.1999.00578.x.

[60] J. Wan, S. Kocak, M.S. Shephard, Automated adaptive 3D forming simulation processes, Eng. Comput. 21 (2005) 47–75, https://doi.org/10.1007/s00366-005-0001-y.

[61] G.R. Johnson, W.H. Cook, Fracture characteristics of three metals subjected to various strains, strain rates, temperatures and pressures, Eng. Fract. Mech. 21 (1985) 31–48, https://doi.org/10.1016/0013-7944(85)90052-9.

[62] W. Tang, X. Guo, J.C. McClure, Heat input and temperature distribution in friction stir welding, J. Mater. Process. Technol. 7 (1998) (1998) 163–172, https://doi.org/10.1106/55TF-PF2G-JBH2-1Q2B.

[63] M.A. Ansari, A. Samanta, R.A. Behnagh, H. Ding, An efficient coupled Eulerian-Lagrangian finite element model for friction stir processing, Int. J. Adv. Manuf. Technol. 101 (2019) 1495–1508, https://doi.org/10.1007/s00170-018-3000-z.

[64] G. Chen, Q. Shi, Y. Li, Y. Sun, Q. Dai, J. Jia, Y. Zhu, J. Wu, Computational fluid dynamics studies on heat generation during friction stir welding of aluminum alloy, Comput. Mater. Sci. 79 (2013) 540–546, https://doi.org/10.1016/j.commatsci.2013.07.004.

[65] Y.H. Yau, A. Hussain, R.K. Lalwani, H.K. Chan, N. Hakimi, Temperature distribution study during the friction stir welding process of Al2024-T3 aluminum alloy, Int. J. Miner. Metall. Mater. 20 (2013) 779–787, https://doi.org/10.1007/s12613-013-0796-2.

[66] J. Zhang, Y. Shen, B. Li, H. Xu, X. Yao, B. Kuang, J. Gao, Numerical simulation and experimental investigation on friction stir welding of 6061-T6 aluminum alloy, Mater. Design 60 (2014) 94–101, https://doi.org/10.1016/j.matdes.2014.03.043.

[67] A.K. Kadian, P. Biswas, A comparative study of material flow behavior in friction stir welding using laminar and turbulent models, J. Mater. Eng. Perform. 24 (2015) 4119–4127, https://doi.org/10.1007/s11665-015-1520-3.

[68] C. Hamilton, M. Kopyscianski, O. Senkov, S. Dymek, A coupled thermal/material flow model of friction stir welding applied to Sc-modified aluminum alloys, Metall. Mater. Trans. A 44 (2013) 1730–1740, https://doi.org/10.1007/s11661-012-1512-y.

[69] C. Hamilton, M.S. Węglowski, S. Dymek, P. Sedek, Using a coupled thermal/material flow model to predict residual stress in friction stir processed AlMg9Si, J. Mater. Eng. Perform. 24 (2015) 1305–1312, https://doi.org/10.1007/s11665-015-1402-8.

[70] G. Chen, S. Zhang, Y. Zhu, C. Yang, Q. Shi, Thermo-mechanical analysis of friction stir welding: a review on recent advances, Acta Metall. Sin. 33 (2020) 3–12, https://doi.org/10.1007/s40195-019-00942-y.

[71] A. Heidarzadeh, S. Mironov, R. Kaibyshev, G. Çam, A. Simar, A. Gerlich, F. Khodabakhshi, A. Mostafaei, D.P. Field, J.D. Robson, A. Deschamps, P.J. Withers, Friction stir welding/processing of metals and alloys: a comprehensive review on microstructural evolution, Prog. Mater. Sci. 117 (2021) 100752, https://doi.org/10.1016/j.pmatsci.2020.100752.

[72] S. Mironov, K. Inagaki, Y.S. Sato, H. Kokawa, *Effect of welding temperature on microstructure of friction-stir welded aluminum alloy 105*0, Metall. Mater. Trans. A 46 (2015) 783–790, https://doi.org/10.1007/s11661-014-2651-0.

[73] A. Kalinenko, I. Vysotskiy, S. Malopheyev, S. Mironov, R. Kaibyshev, Influence of the weld thermal cycle on the grain structure of friction-stir joined 6061 aluminum alloy, Mater. Charact. 178 (2021), 111202, https://doi.org/10.1016/j.matchar.2021.111202.

[74] S. Mironov, Q. Yang, H. Takahashi, I. Takahashi, K. Okamoto, Y.S. Sato, H. Kokawa, Specific character of material flow in near-surface layer during friction stir processing of AZ31 magnesium alloy, Metall. Mater. Trans. A 41 (2010) 1016–1024, https://doi.org/10.1007/s11661-009-0158-x.

[75] S. Mironov, R. Kaibyshev, Abnormal grain growth in fine-grained aluminium produced by friction-stir welding, IOP Conf. Series 672 (2019), 012043, https://doi.org/10.1088/1757-899X/672/1/012043.

[76] R.W. Fonda, K.E. Knipling, Texture development in friction stir welds, Sci. Technol. Weld. Join. 16 (2011) 288–294, https://doi.org/10.1179/1362171811Y.0000000010.

[77] F.J. Humphreys, M. Hatherly, Recrystallization and Related Phenomena, second ed., Elsevier, Oxford, 2004.